8. H. Lammer *et al.*, *Planet. Space Sci.* **54**, 1445 (2006).
9. S. Barabash *et al.*, *Nature* **450**, 650 (2007).
10. The bipolar signature in our rotated coordinate system is in the B_Y component here instead of the B_Z component, as it would be in the usual coordinate system used for a terrestrial magnetotail plasmoid (*18*).
11. T. L. Zhang *et al.*, *Geophys. Res. Lett.* **37**, L14202 (2010).
12. An earlier study found a flux rope in the Venus tail, but reconnection was rejected as a possible source because of the inconsistent orientation of the rope axis (*19*). In our case, the axis is consistent with reconnection. Flux ropes that have been seen on the nightside of Venus are much larger than those in the dayside ionosphere (*20*) and cannot explain these micro-ropes, which appear not to have a magnetic reconnection source (*21*).
13. T. L. Zhang *et al.*, *Nature* **450**, 654 (2007).
14. C. T. Russell, O. Vaisberg, in *Venus*, D. M. Hunten, L. Colin, T. M. Donahue, V. I. Moroz, Eds. (Univ. of Arizona Press, Tucson, AZ, 1983), pp. 873–940.
15. J. L. Phillips, D. L. McComas, *Space Sci. Rev.* **55**, 1 (1991).
16. A. Fedorov *et al.*, *J. Geophys. Res.* **116**, (A7), A07220 (2011).
17. V. Angelopoulos *et al.*, *Science* **321**, 931 (2008).
18. M. B. Moldwin, W. J. Hughes, *J. Geophys. Res.* **96**, (A8), 14051 (1991).
19. J. A. Slavin *et al.*, *Geophys. Res. Lett.* **36**, L09106 (2009).
20. C. T. Russell, R. C. Elphic, *Nature* **279**, 616 (1979).
21. H. Y. Wei, C. T. Russell, T. L. Zhang, M. K. Dougherty, *Icarus* **206**, 174 (2010).
22. T. L. Zhang *et al.*, *Planet. Space Sci.* **54**, 1336 (2006).
23. S. Barabash *et al.*, *Planet. Space Sci.* **55**, 1772 (2007).

Acknowledgments: The work in China was supported by National Natural Science Foundation of China grants 41121003 and 41174156. The work at Graz was supported by Austrian Science Fund (FWF: I429-N16). The work at UCLA was supported by NASA under research grant NNX10AV29G.

23 November 2011; accepted 8 March 2012
Published online 5 April 2012;
10.1126/science.1217013

Ancient Impact and Aqueous Processes at Endeavour Crater, Mars

S. W. Squyres,[1]* R. E. Arvidson,[2] J. F. Bell III,[3] F. Calef III,[4] B. C. Clark,[5] B. A. Cohen,[6] L. A. Crumpler,[7] P. A. de Souza Jr.,[8] W. H. Farrand,[5] R. Gellert,[9] J. Grant,[10] K. E. Herkenhoff,[11] J. A. Hurowitz,[4] J. R. Johnson,[12] B. L. Jolliff,[2] A. H. Knoll,[13] R. Li,[14] S. M. McLennan,[15] D. W. Ming,[16] D. W. Mittlefehldt,[16] T. J. Parker,[4] G. Paulsen,[17] M. S. Rice,[1] S. W. Ruff,[3] C. Schröder,[18] A. S. Yen,[4] K. Zacny[17]

The rover Opportunity has investigated the rim of Endeavour Crater, a large ancient impact crater on Mars. Basaltic breccias produced by the impact form the rim deposits, with stratigraphy similar to that observed at similar-sized craters on Earth. Highly localized zinc enrichments in some breccia materials suggest hydrothermal alteration of rim deposits. Gypsum-rich veins cut sedimentary rocks adjacent to the crater rim. The gypsum was precipitated from low-temperature aqueous fluids flowing upward from the ancient materials of the rim, leading temporarily to potentially habitable conditions and providing some of the waters involved in formation of the ubiquitous sulfate-rich sandstones of the Meridiani region.

After more than 7 years in operation and 33 km of traversing, the Mars Exploration Rover Opportunity has reached Endeavour Crater. Endeavour is ~22 km in diameter and formed in Noachian (*1*) materials that predate the sulfate-rich sedimentary rocks explored by Opportunity for most of its mission (*2*, *3*). Endeavour was chosen as a target because the rocks there record an ancient epoch in martian history, and because orbital infrared data show that phyllosilicate minerals are present in portions of the crater rim (*4*).

Opportunity arrived at Endeavour Crater on sol 2681 (*5*) of its mission, at a low-lying segment of the rim, ~700 m in length, named Cape York (Fig. 1). Shoemaker Ridge (*6*) forms the spine of Cape York and is the type locality for the Noachian materials of the rim, which we call the Shoemaker formation. Opportunity first arrived at Spirit Point, the southern tip of Cape York, and then traversed northward 851 m before stopping at Greeley Haven (*7*) at the northern end of Cape York to spend the martian winter.

Instruments of Opportunity's Athena payload (*8*, *9*) were used to investigate materials within the Shoemaker formation, including the bedrock outcrop Chester Lake (Fig. 2) near the southern end of Shoemaker Ridge, and several bedrock targets near Greeley Haven at the northern end. Although separated by more than half a kilometer, these outcrops are similar in physical appearance and elemental chemistry; we interpret them to represent the dominant surface rock type of Cape York.

Chester Lake and all the rocks near Greeley Haven have similar textures. They are brecciated, with dark, relatively smooth angular clasts up to ~10 cm in size embedded in a brighter, fractured, fine-grained matrix. Some outcrops, notably Chester Lake, show fine-scale lineations in the matrix and alignment of some clasts (Fig. 2). Pancam spectra of the matrix exhibit a gradual decrease in reflectance toward 1000 nm. The clasts can show specular reflections, have a relatively deep absorption at 934 nm, and have a shallower 535-nm absorption than the matrix materials, consistent with relatively unoxidized basaltic material containing low-Ca pyroxene.

The matrix of Chester Lake is easily abraded. A portion of Chester Lake dominated by matrix was abraded to a depth of ~2.5 mm with the rover's Rock Abrasion Tool (RAT). Resistance to abrasion is quantified using specific grind energy, the energy required to abrade away a unit volume of rock. The specific grind energy for Chester Lake was ~1.5 J mm^{-3}. Representative values for weak terrestrial materials are 0.7 to 0.9 J mm^{-3} for chalk and 4.8 to 5.3 J mm^{-3} for gypsum (*10*). Chester Lake is substantially weaker than all but 1 of the 14 diverse rocks abraded by Spirit at Gusev Crater (*11*) but is comparable to the sulfate-rich sandstones at Opportunity's landing site (*12*).

At Chester Lake, we used the Alpha Particle X-Ray Spectrometer (APXS) to measure the elemental composition of both the matrix (after abrasion by the RAT) and one of the clasts. Measurements were also made of three targets near Greeley Haven: Transvaal and Boesmanskop (both matrix) and Komati (a clast). All are similar to one another in composition, and all are similar to the basaltic sand typical of the Meridiani region (Table 1). The major elements (Na, Mg, Al, Si, Ca, and Fe) are mostly within 10 weight percent (wt %) of the basaltic sand composition, and all but a few are within 20 wt %.

Fe/Mn ratios of the matrix range from 40 to 44, and "Mg numbers" [100 × molar Mg/(Mg + Fe)] of all samples range from 41 to 48. These are within the ranges of basaltic meteorites from Mars [Fe/Mn ratios, 36 to 45; Mg numbers, 24 to 68 (fig. S1)] and indicate that any alteration of the protolith of these rocks did not substantially mobilize Mg, Mn, or Fe. P contents are higher than

[1]Department of Astronomy, Cornell University, Ithaca, NY 14853, USA. [2]Department of Earth and Planetary Sciences, Washington University, St. Louis, MO 63031, USA. [3]School of Earth and Space Exploration, Arizona State University, Tempe, AZ 85287, USA. [4]Jet Propulsion Laboratory, California Institute of Technology, Pasadena, CA 91109, USA. [5]Space Science Institute, Boulder, CO 80301, USA. [6]NASA Marshall Space Flight Center, Huntsville, AL 35812, USA. [7]New Mexico Museum of Natural History & Science, Albuquerque, NM 87104, USA. [8]Human Interface Technology Laboratory, University of Tasmania, Launceston TAS 7250, Australia. [9]Department of Physics, University of Guelph, Guelph, Ontario N1G 2W1, Canada. [10]Center for Earth and Planetary Studies, Smithsonian Institution, Washington, DC 20560, USA. [11]U.S. Geological Survey, Astrogeology Science Center, Flagstaff, AZ 86001, USA. [12]Applied Physics Laboratory, Johns Hopkins University, Laurel, MD 20723, USA. [13]Botanical Museum, Harvard University, Cambridge, MA 02138, USA. [14]Department of Civil, Environmental, and Geodetic Engineering, Ohio State University, Columbus, OH 43210, USA. [15]Department of Geosciences, State University of New York, Stony Brook, NY 11794, USA. [16]Astromaterials Research and Exploration Science (ARES), NASA Johnson Space Center, Houston, TX 77058, USA. [17]Honeybee Robotics & Spacecraft Mechanisms Corporation, Pasadena, CA 91103, USA. [18]Universität Bayreuth und Eberhard Karls Universität, 72076 Tübingen, Germany.

*To whom correspondence should be addressed. E-mail: squyres@astro.cornell.edu

those of basaltic sand, and Cr contents are lower. However, these minor elements follow trends of martian basaltic and lherzolitic meteorites (fig. S1), which suggests that igneous fractionation established the major and minor element concentrations.

We interpret all of these rocks to be breccias formed during the Endeavour impact. The compositional similarity to Meridiani basaltic sand is consistent with the view that both materials broadly reflect the composition of the surficial crust in this region.

Although we cannot assess the degree of shock metamorphism of the clasts or the presence of glass in the matrix, we note that the texture of these rocks is similar to the typical texture of suevite breccias (*13*) common in impact settings on Earth and the Moon. For terrestrial suevites, particle shape fabrics have been reported that are oriented radial to the impact point and consequently have been related to the emplacement flow (*14*). The linear fabric in Chester Lake is oriented within ~5° of radial to the center of Endeavour, although we cannot rule out the possibility that this texture is erosional rather than primary.

Near the southern end of Shoemaker Ridge, Opportunity encountered Odyssey crater (Fig. 1). Odyssey is elliptical, ~23 m by 19 m, with its major axis oriented orthogonal to a field of ejecta blocks that extends to the southeast. The ejecta block Tisdale was investigated in detail. Tisdale differs texturally and compositionally from Chester Lake and Greeley Haven rocks. Because it was excavated from Odyssey crater, Tisdale may represent a deeper unit within the Shoemaker formation. Tisdale and other Odyssey ejecta blocks are breccias, with poorly sorted, closely packed, angular to rounded clasts up to several centimeters in size (Fig. 3). Tisdale lacks the extensive fine-grained matrix of Chester Lake and other rocks, and contains lithic fragments over a wide range of grain sizes.

The clasts in Tisdale exhibit spectral variability beyond that expected from discontinuous dust coatings, including positive and negative near-infrared spectral slopes and some 903-nm absorptions. Small, localized spots in Tisdale and nearby rocks exhibit 860- and 535-nm absorptions possibly consistent with a ferric phase and/or minor hydrated Mg/Fe silicates. On the basis of its textural and color properties, we interpret Tisdale as a lithic breccia that is possibly polymict.

APXS measurements of Tisdale were made at three locations on a relatively dust-free vertical face (Table 1). The results are similar to Chester Lake and the Greeley Haven outcrops; however, concentrations of Mg are lower, and concentrations of P and the trace elements Ni, Zn, and Br are higher and quite variable. One location has the highest Zn concentration (~6300 μg g^{-1}) of all analyses from Mars. The Zn and Ni elemental trends are similar to trends in hydrothermally altered rocks around Home Plate in Gusev crater (*15*). Variable P enrichment may result from metasomatism of silicate materials by P-rich hydrothermal solutions (*16*) or acidic solutions dissolving P from source rocks and reprecipitating it (*17*). It is unlikely, however, that the high P content simply reflects an igneous composition different from that of the Chester Lake target material, as the Tisdale targets do not follow typical igneous fractionation trends, such as that defined by martian meteorites (fig. S1C).

It is instructive to compare the rim deposits of Endeavour Crater to those of the comparably sized Ries impact structure in Germany (*18*). At Ries, thin deposits of surficial suevite (*19*), often just a few meters thick, overlie the Bunte Breccia that dominates the impactites of the rim (*20*). The Bunte Breccia is a poorly sorted polymict lithic breccia. It represents the continuous ballistic ejecta deposit and is derived primarily from the uppermost lithologies of the target (*21*). Rounded clasts are common. The surficial suevite that overlies it was deposited late in the impact process, either via fallout from a gaseous ejecta plume (*22*) or as a surface-hugging flow (*23*). We suggest that a similar relationship may hold at Endeavour, with Tisdale representing the main breccia unit of the rim, and Chester Lake and the rocks near Greeley Haven emplaced later in the impact flow.

Tisdale's Zn abundances correlate with both S and P, which suggests that Zn sulfides, sulfates, and/or phosphates could be present. High-Zn materials on Earth are common in settings such as volcanogenic massive sulfide deposits, where hydrothermal circulation has mobilized Zn and caused precipitation of Zn sulfides and development of associated alteration products (*24*). The heating caused by an impact the size of Endeavour is sufficient to cause hydrothermal circulation if water is present (*25*). We suggest that the Zn enrichment in Tisdale could have resulted from such activity. Enrichments of trace metal mineralization by hydrothermal fluids will naturally be localized where fluids readily flow, including fractures, zones with increased permeability, and other void spaces. Highly heterogeneous distribution of secondary mineralization is therefore expected.

When normalized to the average composition of the sulfate-rich sandstones that constitute the Burns formation of the Meridiani plains (*2*, *3*), all rocks of the Shoemaker formation show fractionations among the major elements—for example, high Na/Mg and Al/Mg ratios (fig. S2). Either the Shoemaker formation is not representative of the feedstock for the sulfate-rich grains of the Burns formation, or the alteration process that formed those grains resulted in major compositional changes.

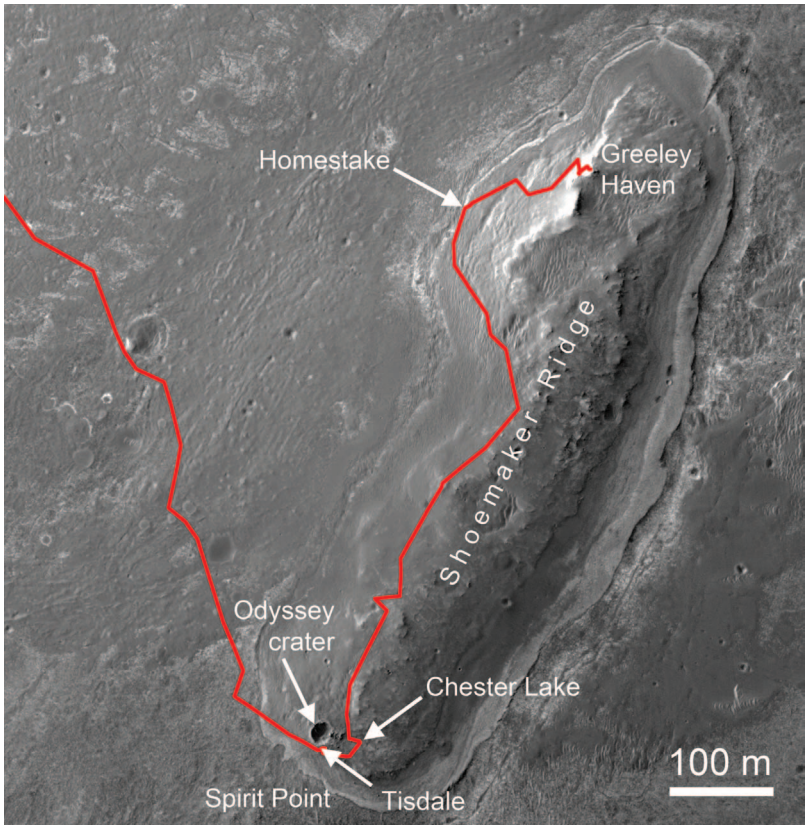

Fig. 1. Opportunity's traverse along the rim segment of Endeavour Crater named Cape York. Major features discussed in the text are indicated. Image was acquired by the Mars Reconnaissance Orbiter HiRISE camera. North is at the top.

The composition of Shoemaker formation rocks is also not a good match to either Bounce Rock (*26*) or Marquette Island (*27*), two basaltic rocks encountered earlier in Opportunity's mission that lie atop Burns formation sandstones. These must be ejecta blocks from distant craters that postdate Endeavour, sampling different crustal materials.

Cape York is encircled by a gently outward-sloping topographic bench ~6 m wide on the west and up to 20 m wide on the east (Fig. 1). The outer part of the bench on the western side exposes bright, thinly bedded sandstones with bedding that dips shallowly toward the plains. These sandstones lie directly above darker granular sedimentary rocks that form the inner portion of the bench. This stratigraphic relationship is interpreted as the unconformable onlapping contact of the Burns formation onto older sedimentary materials shed from the Shoemaker formation. The inner bench materials, in turn, overlie the Noachian breccias that form the lower slopes of Cape York.

Bench materials are cut in many places by bright linear veins. Veins are prominent in the poorly exposed dark sedimentary materials of the inner bench, but occur within the bright outcrops of the basal Burns sandstone as well. Measurements of 37 veins yielded a mean width of 2 cm and a mean exposed length of 33 cm. Most vein orientations lie subparallel to the margins of Cape York.

Opportunity investigated one of these veins, named Homestake (Fig. 4), near the northern end of Cape York. Homestake forms a discontinuous, flat-topped ridge 1 to 1.5 cm wide and ~50 cm long. It stands up to ~1 cm above the surrounding bedrock, which suggests that it is more erosion-resistant than the material into which it was emplaced. Microscopic Imager (MI) images reveal a fine linear texture perpendicular to the trend of the vein (Fig. 4B).

Three separate APXS analyses were conducted on Homestake. All were similar (Table 1), with high abundances of SO_3 and CaO. The SO_3/CaO ratio is within a few percent of stoichiometry for $CaSO_4$, with a possible slight excess of sulfate. Other cations such as Mg, K, Al, and Fe do not show positive correlation with S, but Na does, so a small amount of Na sulfate could be present.

The nonsalt portion of the APXS measurement of Homestake is dominated by Si and Al, which are highly correlated with each other (R^2 = 0.89) and are anticorrelated with S (R^2 = 0.97 to 0.99). MI images (Fig. 4B) show, however, that contaminants must be present in this measurement. Homestake does not fill the ~3.8-cm circular field of view of the APXS, so contamination by background material (mostly dark sand in the MI images) must be present. MI images of Homestake show a mottled upper surface, also suggesting surface contamination.

Modeling the composition of Homestake as a three-component mixture of calcium sulfate,

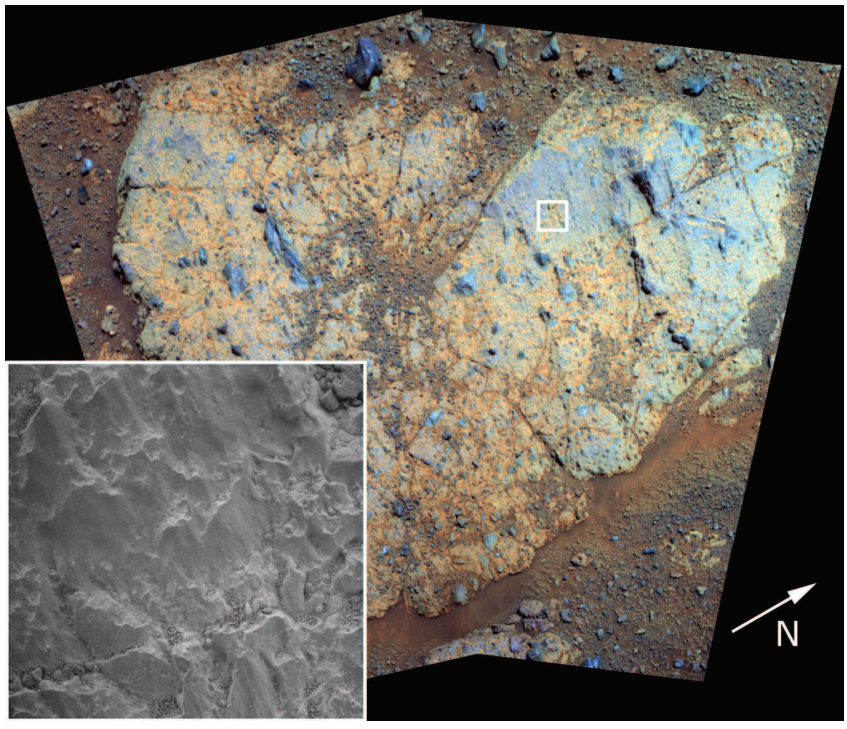

Fig. 2. Pancam false-color mosaic of the rock Chester Lake acquired on sol 2709 using the 753-, 535-, and 432-nm filters, sequence p2394. Scale across the image is ~1 m. Square shows location of MI image (inset) acquired on sol 2713. Scale across MI image is ~3 cm. Clasts in Chester Lake, which stand out in relief, are poorly sorted and irregularly shaped. The MI image shows irregular to cuspate fluting that is aligned with the orientations of elongate clasts.

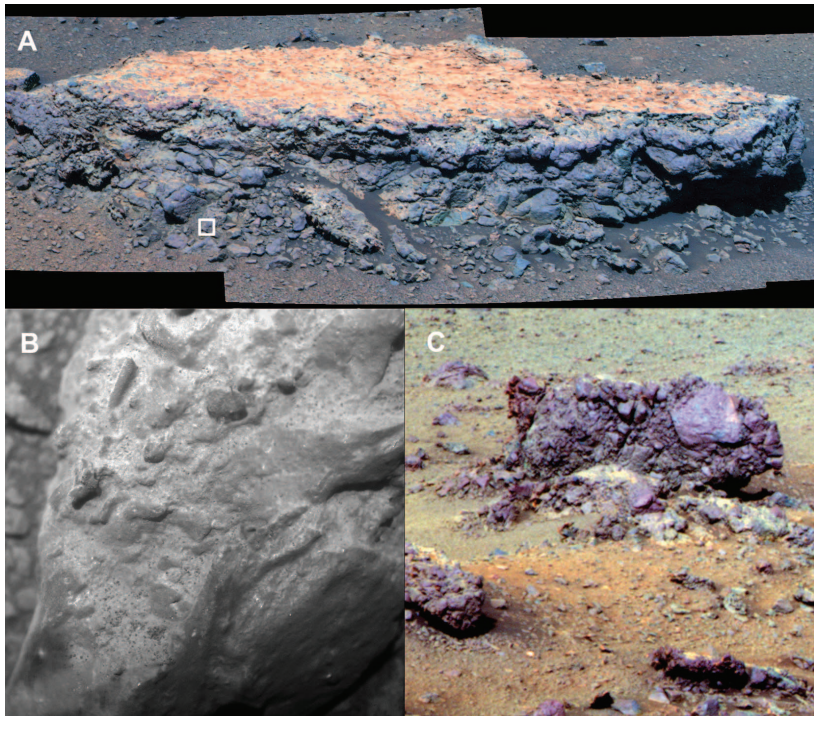

Fig. 3. Ejecta blocks from Odyssey crater. (**A**) Pancam false color image of the block Tisdale acquired on sol 2690 using the 753-, 535-, and 432-nm filters, sequence p2387. Height of Tisdale is ~30 cm. Square shows location of image in (B). (**B**) MI image acquired on sol 2696. Scale across the image is ~2.5 cm. (**C**) Pancam false-color image of the ejecta block Kidd Creek acquired on sol 2694 using the 753-, 535-, and 432-nm filters, sequence p2593. Scale across Kidd Creek is ~1 m. All images show a lithic breccia texture, with clasts ranging in size from tens of centimeters to near the resolution limit of MI images.

typical Meridiani basaltic sand, and typical martian dust, and accounting for the energy dependence of the signal from a thin dust layer, we find that the composition in Table 1 is matched by a mixture of 43% $CaSO_4$, 29% sand, and 28% dust 4 μm thick (*28*). Because the MI images are consistent with these amounts of background sand and surface dust contamination, we conclude that the vein material itself is predominantly $CaSO_4$, with perhaps minor Na_2SO_4, phosphate, and a Cl-containing salt.

Calcium sulfates can have a range of hydration states. APXS data do not constrain the hydration

Table 1. Elemental chemistry as determined by the APXS instrument, under the standard assumption of a homogeneous matrix. Chester Lake is a suevite-like breccia near Spirit Point (Fig. 1), and Transvaal and Boesmanskop are similar rocks near Greeley Haven. Tisdale is a lithic breccia with variable composition. Homestake is the vein in Fig. 4, and Deadwood is the material in which Homestake is emplaced.

	Chester Lake		Transvaal (matrix)	Boesmanskop (matrix)†	Komati (clast)	Tisdale‡	Homestake§	Deadwood	Basaltic sand‖	Dust#	Effective dust**
	Matrix*	Clast									
Weight percent											
Na_2O	2.7 ± 0.2	2.7 ± 0.2	2.3 ± 0.3	2.4 ± 0.4	2.4 ± 0.2	1.8 ± 0.3 2.2 ± 0.3 2.5 ± 0.4	1.6 ± 0.2	2.2 ± 0.2	2.34	2.31	2.28
MgO	8.8 ± 0.1	7.4 ± 0.1	7.5 ± 0.2	8.9 ± 0.2	8.4 ± 0.1	6.2 ± 0.1 6.0 ± 0.1 6.2 ± 0.2	4.7 ± 0.1	5.7 ± 0.1	7.33	7.62	7.18
Al_2O_3	8.8 ± 0.1	10.1 ± 0.2	9.2 ± 0.2	9.5 ± 0.2	9.3 ± 0.2	8.9 ± 0.2 10.0 ± 0.2 10.1 ± 0.2	4.8 ± 0.1	8.3 ± 0.2	9.65	9.21	7.99
SiO_2	45.5 ± 0.4	46.1 ± 0.5	45.9 ± 0.5	45.6 ± 0.5	44.7 ± 0.4	42.6 ± 0.5 46.2 ± 0.5 45.4 ± 0.5	25.3 ± 0.3	44.0 ± 0.5	46.97	45.33	35.29
P_2O_5	1.00 ± 0.08	1.13 ± 0.09	1.04 ± 0.10	1.21 ± 0.09	1.16 ± 0.09	3.14 ± 0.13 1.22 ± 0.10 1.20 ± 0.10	0.78 ± 0.11	1.13 ± 0.10	0.85	0.91	0.73
SO_3	3.1 ± 0.1	4.8 ± 0.1	6.3 ± 0.1	5.6 ± 0.1	5.8 ± 0.1	8.6 ± 0.2 6.0 ± 0.1 6.5 ± 0.1	32.7 ± 0.4	9.2 ± 0.1	4.68	7.23	5.02
Cl	0.9 ± 0.0	1.0 ± 0.0	1.0 ± 0.0	1.0 ± 0.0	0.9 ± 0.0	1.2 ± 0.0 0.9 ± 0.0 1.0 ± 0.0	1.0 ± 0.0	1.1 ± 0.0	0.59	0.81	0.48
K_2O	0.41 ± 0.06	0.46 ± 0.06	0.49 ± 0.06	0.51 ± 0.06	0.58 ± 0.06	0.43 ± 0.07 0.50 ± 0.07 0.53 ± 0.07	0.27 ± 0.06	0.62 ± 0.07	0.51	0.5	0.19
CaO	6.8 ± 0.1	7.1 ± 0.1	6.6 ± 0.1	5.7 ± 0.1	6.1 ± 0.1	7.1 ± 0.1 6.8 ± 0.1 5.9 ± 0.1	22.0 ± 0.2	6.7 ± 0.1	7.38	6.66	2.03
TiO_2	1.09 ± 0.08	1.15 ± 0.08	1.11 ± 0.08	1.03 ± 0.08	1.08 ± 0.07	0.99 ± 0.08 1.05 ± 0.10 1.05 ± 0.09	0.27 ± 0.06	0.98 ± 0.08	0.9	0.99	0.22
Cr_2O_3	0.25 ± 0.03	0.27 ± 0.04	0.28 ± 0.04	0.25 ± 0.04	0.18 ± 0.03	0.16 ± 0.04 0.27 ± 0.04 0.23 ± 0.04	0.13 ± 0.04	0.30 ± 0.04	0.39	0.34	0.05
MnO	0.48 ± 0.02	0.63 ± 0.02	0.41 ± 0.02	0.41 ± 0.02	0.59 ± 0.01	0.38 ± 0.02 0.38 ± 0.02 0.23 ± 0.02	0.15 ± 0.01	0.22 ± 0.02	0.39	0.36	0.04
FeO	20.1 ± 0.1	17.0 ± 0.2	17.8 ± 0.2	17.6 ± 0.2	18.7 ± 0.1	17.6 ± 0.2 18.0 ± 0.2 18.8 ± 0.2	6.4 ± 0.1	19.4 ± 0.2	17.57	17.59	1.62
Concentration (μg g^{-1})											
Ni	482 ± 54	461 ± 65	565 ± 64	615 ± 65	461 ± 48	950 ± 84 1405 ± 95 2030 ± 108	36 ± 83	410 ± 62	349	486	53
Zn	246 ± 18	244 ± 23	294 ± 23	350 ± 25	266 ± 15	6267 ± 108 1798 ± 58 710 ± 42	121 ± 20	521 ± 29	199	390	29
Br	124 ± 18	68 ± 19	139 ± 21	153 ± 22	229 ± 19	779 ± 35 722 ± 34 377 ± 29	68 ± 19	301 ± 25	24	31	1

*Sample abraded with the RAT. †Sample brushed with the RAT. ‡Measurements at three different locations on a relatively dust-free vertical face. §Average of three measurements. ‖Typical Meridiani basaltic sand composition. #Typical martian dust used in geochemical modeling of Homestake. **Effective composition of a layer of dust 4 μm thick, taking into account the energy dependence of the APXS signal.

state of Homestake because of the instrument's inability to detect H and the confounding effects of background and contamination discussed above. However, Pancam's longest-wavelength filter (1009 ± 19 nm) provides the ability to detect remotely and map spatially certain hydrated minerals, based on the presence of the $2\nu_1 + \nu_3$ H_2O combination absorption band and/or the $3\nu_{OH}$ overtone absorption band centered near ~1000 nm in many minerals containing bound H_2O and/or OH^- (*29*, *30*).

Figure 5A shows that hydrated mineral signatures [characterized by four total spectral parameters (*30*), including steeply negative slopes from 934 to 1009 nm] are detected in Homestake. These spectral features occur in three separate unsaturated Pancam observations acquired at different viewing geometries and incidence angles, convincing us that the signature is due to hydration in Homestake rather than any instrumental, calibration, or viewing geometry artifact (*30*). The magnitude of the hydration signature and the albedo both increased after Opportunity drove over and exposed fresh crushed parts of Homestake; this suggests that the hydrated material is not a superficial coating or rind, but rather a component of the bulk volume of the vein material.

Laboratory reflectance spectra of calcium sulfates convolved to Pancam bandpasses (Fig. 5B) suggest that the hydration signature is consistent with gypsum ($CaSO_4 \cdot 2H_2O$), but not anhydrite ($CaSO_4$) or bassanite ($CaSO_4 \cdot 0.5H_2O$). Anhydrite lacks a hydration band, and the weak bassanite hydration band is centered near ~950 nm, between Pancam's two longest-wavelength band centers.

Gypsum veins have been reported in a variety of settings on Earth, where their formation is invariably attributed to precipitation from relatively low-temperature (less than ~60°C) water in fractures (*31*–*34*). Vein growth is often antitaxial, with nucleation occurring at the vein-wall interface. Crystals precipitated in such settings are commonly fibrous, with long axes that track the opening trajectory of the fracture (*34*–*36*); fibers therefore form perpendicular to the vein axis when vein growth occurs in extension fractures. We suggest that the transverse lineations seen in MI images of Homestake are remnants of such a texture. The orientations of the veins themselves suggest that the rocks of the bench surrounding Cape York were subjected to horizontal tension perpendicular to the bench margins at the time of vein emplacement, perhaps related to sediment compaction, dewatering, and settling.

Homestake was emplaced in the darker inner unit of the bench surrounding Cape York. The rock of this unit is platy in appearance, with millimeter-scale layering that is poorly exposed but shows locally varying strikes and dips. Its elemental composition, measured at a location named Deadwood (Table 1), is similar to that of rocks of the Shoemaker formation, although without strong Zn and Ni enrichments. From its elevated Ca and S concentrations, Deadwood also appears to contain a small amount (~10%) of Homestake-like material. Typical Meridiani basaltic sand could constitute up to 30% of the total (MI images suggest 20 to 30% contamination), but not more because the Mn/Fe ratio would become untenably low. We interpret Deadwood to be a clastic sedimentary rock dominated by grains from the Shoemaker formation, with minor

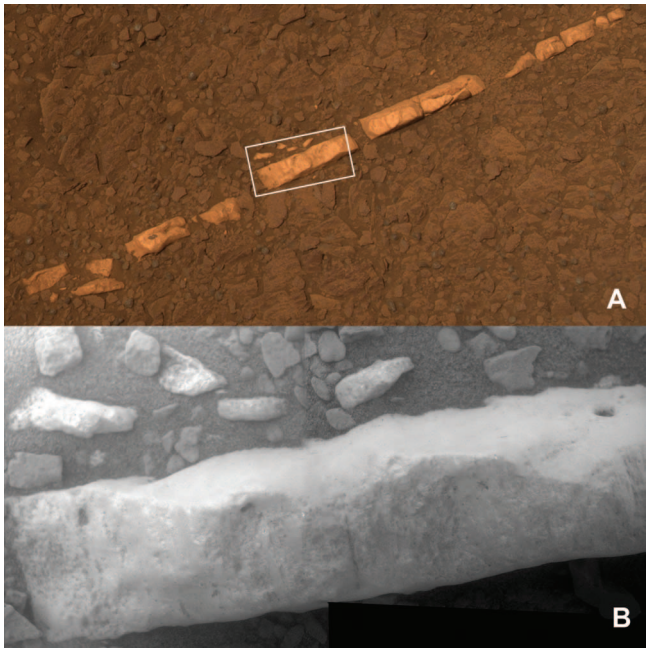

Fig. 4. (**A**) Pancam approximate true-color image of the vein Homestake acquired on sol 2769 using the 753-, 535-, and 432-nm filters, sequence p2574. Scale across the image is ~40 cm. Rectangle shows location of image in (B). (**B**) MI mosaic acquired on sol 2766.

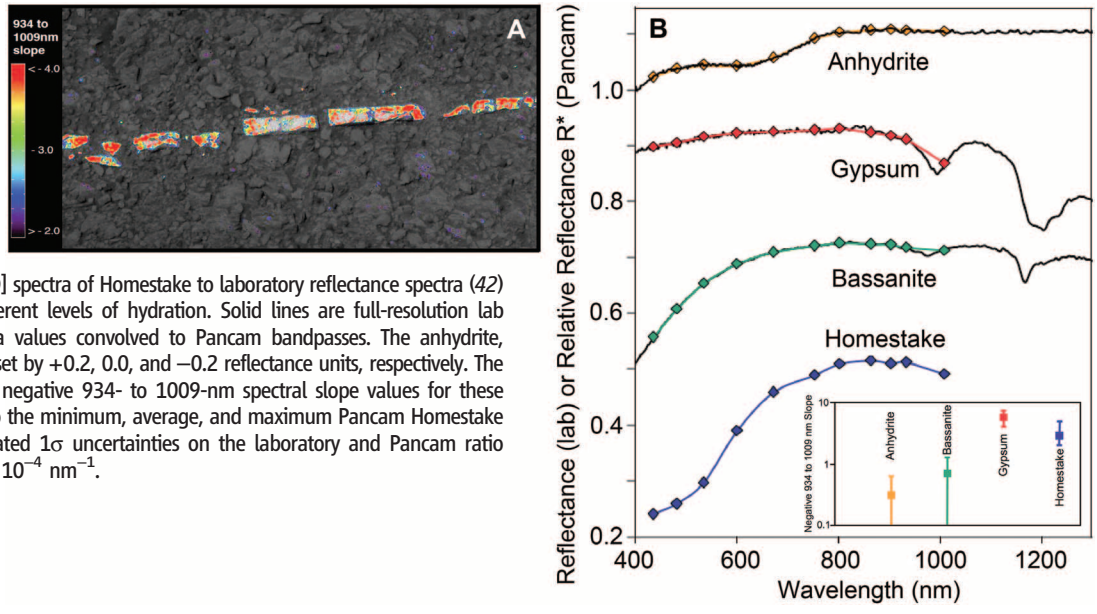

Fig. 5. (**A**) Pancam "hydration signature" data overlain on a 754-nm image of Homestake acquired on sol 2769, sequence p2574. Colors indicate regions where the 934- to 1009-nm spectral slope is negative and where four other hydration signature spectral parameters (*29*) are also met. (**B**) Comparison of Pancam relative reflectance [*R** (*41*)] spectra of Homestake to laboratory reflectance spectra (*42*) of three calcium sulfates with different levels of hydration. Solid lines are full-resolution lab spectra; points indicate lab spectra values convolved to Pancam bandpasses. The anhydrite, gypsum, and bassanite data are offset by +0.2, 0.0, and −0.2 reflectance units, respectively. The inset shows the magnitude of the negative 934- to 1009-nm spectral slope values for these three mineral samples compared to the minimum, average, and maximum Pancam Homestake values. Error bars represent estimated 1σ uncertainties on the laboratory and Pancam ratio values. Logarithmic plot; units are 10^{-4} nm^{-1}.

$CaSO_4$, perhaps as cement. Basaltic sand contaminates the APXS measurement but does not change this interpretation.

The key stratigraphic and crosscutting relationships along the western margin of Cape York are depicted in Fig. 6. We interpret the inner portion of the bench, characterized by Deadwood, to be the first sedimentary unit to form on Endeavour's rim, dominated by material shed from the Cape York breccias. This material, and the basal Burns formation sandstone that unconformably overlies it, were subsequently cut by fractures that were filled by gypsum precipitated from sulfate-rich fluids generated within the nearby Noachian crust. These fluids were likely at a low temperature (if hydrothermal, they were distal), because anhydrite would be expected otherwise. In pure water the gypsum/anhydrite conversion temperature is ~40° to 60°C, and in concentrated brines it can be substantially lower (*37*). Calcium sulfate was precipitated closest to the Noachian source rocks, rather than other sulfates (e.g., $MgSO_4 \cdot nH_2O$; $FeSO_4 \cdot nH_2O$) or chlorides, because of its lower solubility. Some gypsum was also precipitated as cement in the bedrock. Unlike the Burns formation sulfates that dominate the Meridiani plains and are rich in jarosite (*2*, *3*), the gypsum of Homestake did not require acidic fluids for its formation. We suggest, however, that the fluids from which the gypsum was precipitated may have been a contributor to the overall hydrologic budget responsible for formation of the Meridiani sulfate sandstones.

The absence of substantial deformation of the veins suggests that there has been minimal transformation between gypsum and anhydrite since emplacement. The molar volumes of these minerals differ by a factor of ~1.6; in terrestrial settings, such transformations typically produce complex deformation features (*38*). The absence of gypsum-anhydrite transformations further suggests that these rocks remained at relatively low temperatures since vein emplacement.

Development of the materials investigated at Endeavour began with an impact into basaltic rocks, producing breccias with a stratigraphy similar to that observed at some comparably sized terrestrial impact craters. Degradation and shedding of these breccias formed thin sedimentary materials immediately surrounding Cape York, over which the basal Burns formation sandstones were unconformably deposited. Emplacement of the gypsum veins then took place, postdating the earliest Burns formation sandstones but probably predating much of the rest of the Burns formation stratigraphy encountered by Opportunity.

The ubiquity of impact breccia at Cape York contrasts with the only other Noachian terrain explored in situ, the Columbia Hills in Gusev Crater. The rover Spirit encountered great lithologic diversity there, including materials interpreted as impact ejecta (*11*). However, none were breccias, and none had the lateral extent of the Shoemaker formation. We suggest that the difference can be attributed to Opportunity's sampling of the rim deposits of a single large crater, rather than Spirit's sampling of more distal ejecta from multiple impacts.

The gypsum veins at Cape York provide clear evidence for relatively dilute [water activity $a_w \approx 0.98$ (*39*)] water at a moderate temperature, perhaps supporting locally and transiently habitable environments. More broadly, rocks at Cape York appear to record early events in a transition from (commonly) hydrothermal waters that altered basaltic crust to phyllosilicates (*40*) to sulfate-charged ground waters that generated salt-rich sandstones deposited widely over the Meridiani plains and elsewhere.

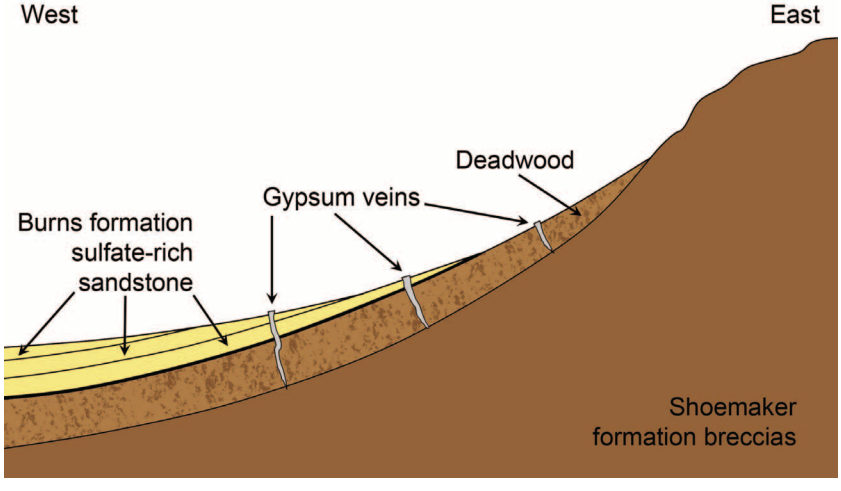

Fig. 6. Schematic east-west cross section, with large vertical exaggeration, through the western flank of Cape York. Materials shed from the Shoemaker formation breccias form the lowest sedimentary unit, which includes Deadwood. This unit is overlain by the sulfate-rich sandstones of the Burns formation; the heavy line separating them represents an unconformity. The Deadwood unit and the basal portion of the Burns formation closest to Cape York are cut by fractures; these fractures are filled with gypsum that was precipitated from waters arising from the underlying breccias.

References and Notes

1. The Noachian is a geologic system on Mars representing the oldest period of the planet's geologic history, characterized by high impact rates.
2. S. W. Squyres *et al.*, *J. Geophys. Res.* **111**, E12S12 (2006).
3. R. E. Arvidson *et al.*, *J. Geophys. Res.* **116**, E00F15 (2011).
4. J. J. Wray *et al.*, *Geophys. Res. Lett.* **36**, L21201 (2009).
5. A sol is defined as one martian solar day.
6. Shoemaker Ridge is named to honor the late Eugene M. Shoemaker, one of the founders of planetary geoscience.
7. Greeley Haven is named to honor the late Ronald Greeley, distinguished planetary scientist and member of the Athena Science Team.
8. S. W. Squyres *et al.*, *J. Geophys. Res.* **108**, 8062 (2003).
9. The Miniature Thermal Emission Spectrometer (Mini-TES) was not used for this investigation because of temperature-related instrument degradation and optically thick dust on its mirrors accumulated during a prior global dust storm. The Mössbauer Spectrometer was not used because of the decay of its ^{57}Co radiation source.
10. T. Myrick *et al.*, in *Proceedings of AIAA Space 2004 Conference and Exhibit* (American Institute of Aeronautics and Astronautics, Reston, VA, 2004), pp. 1–11.
11. S. W. Squyres *et al.*, *J. Geophys. Res.* **111**, E02S11 (2006).
12. R. E. Arvidson *et al.*, *Science* **306**, 1730 (2004).
13. D. Stöffler, R. A. F. Grieve, in *Metamorphic Rocks: A Classification and Glossary of Terms, Recommendations of the International Union of Geological Sciences*, D. Fettes, J. Desmons, Eds. (Cambridge Univ. Press, Cambridge, 2007), chap. 2.11.
14. C. Meyer, M. Jebrak, D. Stoffler, U. Riller, *Geol. Soc. Am. Bull.* **123**, 2312 (2011).
15. M. E. Schmidt *et al.*, *J. Geophys. Res.* **113**, E06S12 (2008).
16. C. G. Wheat, R. A. Feely, M. J. Motti, *Geochim. Cosmochim. Acta* **60**, 3593 (1996).
17. E. S. Deevey Jr., *Sci. Am.* **223**, 148 (1970).
18. J. Pohl *et al.*, in *Impact and Explosion Cratering*, D. J. Roddy, R. O. Pepin, R. B. Merrill, Eds. (Pergamon, New York, 1977), pp. 343–404.
19. W. von Engelhardt *et al.*, *Meteoritics* **30**, 279 (1995).
20. W. von Engelhardt, *Tectonophysics* **171**, 250 (1990).
21. F. Hörz, R. Ostertag, D. A. Rainey, *Rev. Geophys.* **21**, 1667 (1983).
22. W. von Engelhardt, *Meteorit. Planet. Sci.* **32**, 545 (1997).
23. H. E. Newsom, G. Graup, T. Sewards, K. Keil, *J. Geophys. Res.* **91**, E239 (1986).
24. J. M. Franklin, J. W. Lydon, D. F. Sangster, *Econ. Geol.* (75th anniv. volume), 485 (1981).
25. J. A. Rathbun, S. W. Squyres, *Icarus* **157**, 362 (2002).
26. J. Zipfel *et al.*, *Meteorit. Planet. Sci.* **46** (suppl. S1), A1 (2011).
27. D. W. Mittlefehldt *et al.*, *Lunar Planet. Sci.* **41**, 2109 (2009).
28. A 4-μm-thick dust layer is the simplest model that fits the APXS data; the actual dust coating is probably discontinuous and variable in thickness.
29. A. Wang *et al.*, *J. Geophys. Res.* **113**, E12S40 (2008).
30. M. S. Rice *et al.*, *Icarus* **205**, 375 (2010).
31. S. Taber, *J. Geol.* **26**, 56 (1918).
32. T. C. Gustavson *et al.*, *J. Sed. Res. A* **64**, 88 (1994).
33. M. El Tabakh *et al.*, *J. Sed. Res.* **68**, 88 (1998).
34. S. L. Philipp, *Geol. Mag.* **145**, 831 (2008).
35. D. W. Durney, J. G. Ramsay, in *Gravity and Tectonics*, K. A. de Jong, R. Scholten, Eds. (Wiley, New York, 1973), pp. 67–96.
36. P. D. Bons, M. Montenari, *J. Struct. Geol.* **27**, 231 (2005).

37. D. Freyer, W. Voigt, *Monatsh. Chem.* **134**, 693 (2003).
38. W. M. Bundy, *J. Sed. Res* **26**, 240 (1956).
39. N. J. Tosca, A. H. Knoll, S. M. McLennan, *Science* **320**, 1204 (2008).
40. B. L. Ehlmann *et al.*, *Nature* **479**, 53 (2011).
41. J. F. Bell III *et al.*, *J. Geophys. Res.* **108**, 8063 (2003).
42. R. N. Clark *et al.*, U.S. Geological Survey, USGS Digital Spectral Library 06 (2007); http://speclab.cr.usgs.gov/spectral.lib06.

Acknowledgments: This research was carried out for the Jet Propulsion Laboratory, California Institute of Technology, under a contract with NASA.

Supplementary Materials
www.sciencemag.org/cgi/content/full/336/6081/570/DC1
Figs. S1 and S2
References (*43*–*96*)

13 February 2012; accepted 3 April 2012
10.1126/science.1220476

21st-Century Evolution of Greenland Outlet Glacier Velocities

T. Moon,[1,2]* I. Joughin,[2] B. Smith,[2] I. Howat[3,4]

Earlier observations on several of Greenland's outlet glaciers, starting near the turn of the 21st century, indicated rapid (annual-scale) and large (>100%) increases in glacier velocity. Combining data from several satellites, we produce a decade-long (2000 to 2010) record documenting the ongoing velocity evolution of nearly all (200+) of Greenland's major outlet glaciers, revealing complex spatial and temporal patterns. Changes on fast-flow marine-terminating glaciers contrast with steady velocities on ice-shelf–terminating glaciers and slow speeds on land-terminating glaciers. Regionally, glaciers in the northwest accelerated steadily, with more variability in the southeast and relatively steady flow elsewhere. Intraregional variability shows a complex response to regional and local forcing. Observed acceleration indicates that sea level rise from Greenland may fall well below proposed upper bounds.

Changes in glacier dynamics contribute to roughly half of the Greenland Ice Sheet's current mass loss (~250 Gt/year, equivalent to 0.6 mm/year sea level rise) (*1*, *2*), largely through thinning and increased calving as glaciers have sped up. Large changes in ice dynamics have been observed (*3*), but were not accounted for in early models and led to the inability to quantify uncertainty of 21st-century sea level rise in the Intergovernmental Panel on Climate Change's (IPCC's) Fourth Assessment (*4*). Although multiglacier speedups have been linked to recent warming in Greenland (*5*–*7*), the exact connection to climate change is poorly known, but may be related to processes controlled by ice-ocean interaction (*8*–*10*). A firm understanding of the processes driving recent change, which is needed to improve predictions of sea level rise, requires a better characterization of the temporal and spatial patterns of ice flow across the ice sheet.

Despite the need for comprehensive data, recent studies of glacier velocity in Greenland are limited in spatial and temporal resolution. For Jakobshavn Isbræ, Helheim Gletscher, and Kangerdlugssuaq Gletscher, three of Greenland's fastest outlet glaciers, velocity is relatively well documented (*3*, *11*, *12*). For most of Greenland's other 200+ outlet glaciers, however, observation has been limited to ~5-year sampling on an ice-sheet–wide scale (*13*, *14*) or smaller regions with more frequent sampling (*7*). Where comprehensive records exist, they have been used to focus on aggregate discharge rather than regional variability (*2*). We present a decade-long record, with annual sampling for the latter half, to examine decadal-scale trends and regional and local interannual variation, and to inform predictions of sea level rise.

To create this record, we produced velocity maps for winter 2000 to 2001 (referred to as 2000) and annually for each winter from 2005 to 2006 through 2010 to 2011 (referred to using the earlier year for the map), using synthetic aperture radar data from the Canadian Space Agency's RADARSAT-1, German TerraSAR-X, and Japanese Advanced Land Observation Satellite (ALOS) (table S1). We used a combination of speckle-tracking and interferometric algorithms to estimate ice-flow velocity (*14*, *15*). Coverage for each year is almost complete, with some unavoidable gaps, primarily in the south, due to satellite acquisition limits.

Of the 206 largest Greenland outlet glaciers, 178 have adequate temporal coverage for 2000 to 2005, and 195 have sufficient data for 2005 to 2010 (Fig. 1) (*16*). We divided these glaciers into several categories. First, we identified land-terminating, ice-shelf–terminating (ice shelf >10 km long), and low-velocity marine-terminating (mean velocity <200 m/year) glaciers (55 total). Next, glaciers with highly variable behavior were separated to avoid misrepresenting large variations as consistent trends (*16*). This included glaciers such as Harald Moltke Bræ (fig. S1), where apparent surge behavior produces erratic changes (*17*). The final group consisted of fast-flow marine-terminating glaciers that we fit with linear regressions for all available data for 2000 to 2005 (111 glaciers) and 2005 to 2010 (123 glaciers) to evaluate trends and fill data gaps (figs. S2 and S3).

Our record reveals the complexity of Greenland's ice flow. Greenland's largest land-terminating glaciers are located primarily along the southwest coast, with a few in the northeast (Fig. 1). Nearly all flow at peak velocities between 10 and 100 m/year, so that annual changes of 10 to 30 m/year produce large long-term trends (>15% change over 5 years). Most (70%) of the land-terminating glaciers with a notable trend slowed during 2005 to 2010—a continuing trend for half of them. The scale of these changes, however, is close to the measurement error and seasonal variability (*11*) and orders of magnitude smaller than changes seen on many fast-flowing glaciers. The one outlier, Frederikshab Isblink (fig. S1), has a large lobe-shaped terminus that is primarily land-terminating, but with one segment of lake-terminating ice front. The velocity field suggests that this segment helps the glacier maintain a higher peak velocity (~270 m/year) than other land-terminating glaciers and hints at the importance of a calving terminus in maintaining fast ice flow.

Ice-shelf–terminating glaciers (Fig. 1) have mean velocities (300 to 1670 m/year) that are generally slower than those of other marine-terminating glaciers (total mean: 1890 m/year), but most show negligible change for 2000 to 2010. The most notable change occurred on Hagen Bræ (from 50 m/year in 2000 to 650 m/year in 2007), a previously identified surge-type glacier (*18*).

Surge-type glaciers occur mostly in the northwest, north, and east (*18*, *19*). In several cases, 1- or 2-year velocity changes suggest surge-type behavior, as observed on Harald Moltke Bræ (high speed in 2005), where surges have been recorded before, and Adolf Hoel Gletscher (low speed in 2007) (fig. S1) and Kangilerngata sermia (low speed in 2005), where earlier surges have not been recorded. Other glaciers where surges have been observed previously, including Storstrommen and L. Bistrup Bræ (*18*) and Sortebræ (*20*), maintained quiescent speeds over the past decade.

Most glaciers in east Greenland are marine-terminating, but have substantially slower mean velocities (1040 m/year) relative to southeast (2830 m/year) or northwest (1630 m/year) marine-terminating glaciers. This is consistent with the lower regional discharge from this low accumulation area (*21*). As a group, eastern glaciers showed only negligible changes from 2000 to

[1]Earth and Space Sciences, University of Washington, Seattle, WA 98195, USA. [2]Polar Science Center, Applied Physics Lab, University of Washington, Seattle, WA 98105, USA. [3]School of Earth Sciences, Ohio State University, Columbus, OH 43210, USA. [4]Byrd Polar Research Center, Ohio State University, Columbus, OH 43210, USA.

*To whom correspondence should be addressed. E-mail: twilap@uw.edu